



Yaochong Mo deposit, a low-F porphyry Mo deposit from the Qinling-Dabie orogenic belt



Mei Mi ^{a,*}, Cong-ying Li ^a, Wei-dong Sun ^{c,d,f}, Deng-feng Li ^b, Chao-hui Zhu ^e

^a CAS Key Laboratory of Mineralogy and Metallogeny, Guangzhou Institute of Geochemistry, Chinese Academy of Sciences, Guangzhou 510640, China

^b School of Marine Sciences, Sun Yat-sen University, Guangzhou 510006, China

^c CAS Center for Excellence in Tibetan Plateau Earth Sciences, Chinese Academy of Sciences, Beijing 100101, China

^d Center of Deep Sea Research, Institute of Oceanology, Chinese Academy of Sciences, Qingdao 266071, China

^e Scientific Research Institution of State Land Resources, Henan Province, Zhenzhou 450053, China

^f Laboratory for Marine Mineral Resources, Qingdao National Laboratory for Marine Science and Technology, Qingdao 266237, China

ARTICLE INFO

Article history:

Received 7 October 2016

Received in revised form 14 March 2017

Accepted 31 March 2017

Available online 5 May 2017

Keywords:

Porphyry molybdenum
LA-ICP-MS

Zircon

Apatite

Low-F

Qingling-Dabie

ABSTRACT

The Qinling-Dabie orogenic belt is the largest Mo mineralization belt in the world. The Yaochong porphyry Mo deposit is located in the northwest Dabie Mountains, with a proven reserve of 51 kt Mo metal at an average grade of 0.058%. Here we report geochronology and geochemistry results of the Yaochong porphyry Mo deposit. Zircon U-Pb LA-ICP-MS dating shows that the Yaochong porphyry dykes and a hidden intrusion formed at 135 Ma and 140 Ma, respectively, which are consistent with Early Cretaceous Mo mineralization events in the Qinling-Dabie orogenic belt. Zircon grains from the Yaochong porphyry dykes (2–1788) and the hidden intrusion from drill holes (41–1940) have highly variable Ce⁴⁺/Ce³⁺ values. It is very likely that both the intrusion and the dykes have experienced high oxygen fugacity, but was partially reduced through assimilation. Apatite grains from the Yaochong porphyry and the intrusion are characterized by high but variable F concentrations and low Cl concentrations, suggesting that they formed in an F-enriched environment with high F/Cl components in the magma source. The Ti-in zircon temperatures of the porphyry dykes range from 700 to 710 °C, whereas the average temperature of the buried intrusion nearby is 675 °C. Yaochong porphyry shows geochemical and petrologic characteristics similar to those of low F stockwork type porphyry Mo deposit in North America, which may be inherited from the Dabie suture zone.

© 2017 Elsevier B.V. All rights reserved.

1. Introduction

There are two types of porphyry Mo deposits, low-F and Climax (high-F) types (Carten et al., 1993; Sillitoe, 1980; White, 1981; Sun et al., 2016). Generally, low-F porphyry Mo deposits do not form in the same regions or tectonic environments as Climax-type. Low-F porphyry-Mo deposits on the west coast of North America formed over a wider time interval from 144 to 8 Ma, with about half of the reserves formed in the Cenozoic (Ludington et al., 2009a,b). Climax-type porphyry deposits are associated with alkaline rocks. In contrast, low-F porphyry-Mo deposits are mostly associated with calc-alkaline granitic to granodioritic porphyries. They are also less felsic, with lower F, Nb, and Ta concentrations, and systematically lower Mo grades (0.05–0.2% Mo) than those of the Climax-type (0.1–1% Mo).

Qinling-Dabie orogenic belt is the largest Mo belt in the world with proven reserves of more than seven million tonnes of Mo metal (Li et al., 2012a,b, 2013; Stein et al., 1997; Zhang et al., 2014; Chen et al., 2017). The formation of such a large porphyry Mo belt is still debated. Previous studies suggested that Shapinggou is a Climax-type porphyry Mo deposit (Zhang et al., 2014), whereas Qian'echong is a low-F porphyry Mo deposit (Mi et al., 2015a,b; Yang et al., 2012). With the exception of these two cases, there is no classification for porphyry Mo deposits in the Qinling-Dabie orogenic belt. Here we show that Yaochong is a low-F porphyry Mo deposit. This implies that the Qinling-Dabie porphyry Mo belt is comparable to those in western America, providing a good opportunity to better understand porphyry Mo deposits in general.

2. Geologic backgrounds

The Central Orogenic Belt is located between the North China and Yangtze Cratons (Fig. 1). The northwest Dabie Mountains is

* Corresponding author.

E-mail address: meimei@gig.ac.cn (M. Mi).

the middle part of the Qinling-Dabie-Sulu orogenic belt, located in the eastern Central Orogenic Belt. The Dabie Mountains are famous for the Triassic ultra-high-pressure metamorphic (UHPM) rocks and situated to the south of the Luanchuan, north of the Xiangfan-Guangji faults (Fig. 1) (Li et al., 1993, 2014; Zheng et al., 2003; Zheng, 2008). The suture between these two blocks is located along the Xiaotian-Mozitan Fault and the southern margin of the Huwan Formation (Sun et al., 2002b). Triassic magmatism is not well developed in the Dabie Mountains, with only minor foliated garnet-bearing granite veins (Zhang et al., 2009), which is dramatically different from the Cretaceous magmatism in the Dabie Mountains (Huang et al., 2008; Ling et al., 2011a; Zhao et al., 2011; Wang et al., 2007). Several mineralized small Yanshanian granitic stocks, such as Tianmugou, Xiaofan, Mushan, Dayinjian, Tangjiaping and Shapinggou, are also emplaced in the Dabie Mountains and associated with large porphyry Mo deposits (Fig. 1).

The Yaochong Mo deposit is situated in the western Dabie Mountain, ca. 6 km northeast of the Xinxiang County, Henan Province (China) (Fig. 1). The geological units from northeast to southwest are the Carboniferous Meishan Group, the Devonian-Triassic Xinyang Group, the 0.85–0.43 Ga Suijiahe Group, the >0.75 Ga Dabie/Tongbai complex, Neoproterozoic Suixian and Hong'an Group and some Mesozoic volcanic rocks in the northeastern part.

The Dabie/Tongbai complex includes Neoproterozoic granitic gneisses and supra crustal rocks. The granitic gneisses are widespread in the region and intruded by the Late Paleozoic plutonic rocks, Cretaceous intrusions and porphyry dykes (this study),

which were emplaced in the north of the deposit, and their contact zones were partly altered. These plutons may be chronologically surmised as: 1) the main Late Paleozoic intrusions, which are gneissic fine-grained eclogites-containing (<5%) granite, with magnetite as accessory mineral (Li et al., 2001). 2) The Early Cretaceous intrusion comprised of quartz diorite, fine- or medium-grained monzogranite, porphyry stocks and dykes, typically with multi-stage intrusions (Guo et al., 2004) (Fig. 2). Diorite or plagioclase amphibolite enclaves may be observed in the quartz diorite and monzogranite. 3) The porphyry stocks/dykes are NWW- or E-trending and emplaced along faults, which are several hundred meters long and a few or tens of meters wide. These stocks/dykes are comprised of K-feldspar, plagioclase, quartz with minor epidote and biotite, associated with Mo mineralization (Li et al., 2012a,b).

3. Regional and ore geology

The Yaochong porphyry Mo deposit in Xinxiang County, Henan Province, China, is located in the Hong'an terrane, the western part of the Dabie orogen. The Dabie orogen is part of a >1500 km long, Triassic continental collision belt between the North China Block and the South China Block. The Yaochong porphyry deposit contains four individual orebodies that are mainly hosted in Neoproterozoic granitic gneisses. The total reserve is 88 Mt ores at an average grade of 0.058% Mo. The main ore body is about 960 m long and 480–800 m wide, with a lenticular or sheet like shape. It dips northward or northwestward, with edges branching and pinching out (Wang et al., 2013). The main ore minerals are

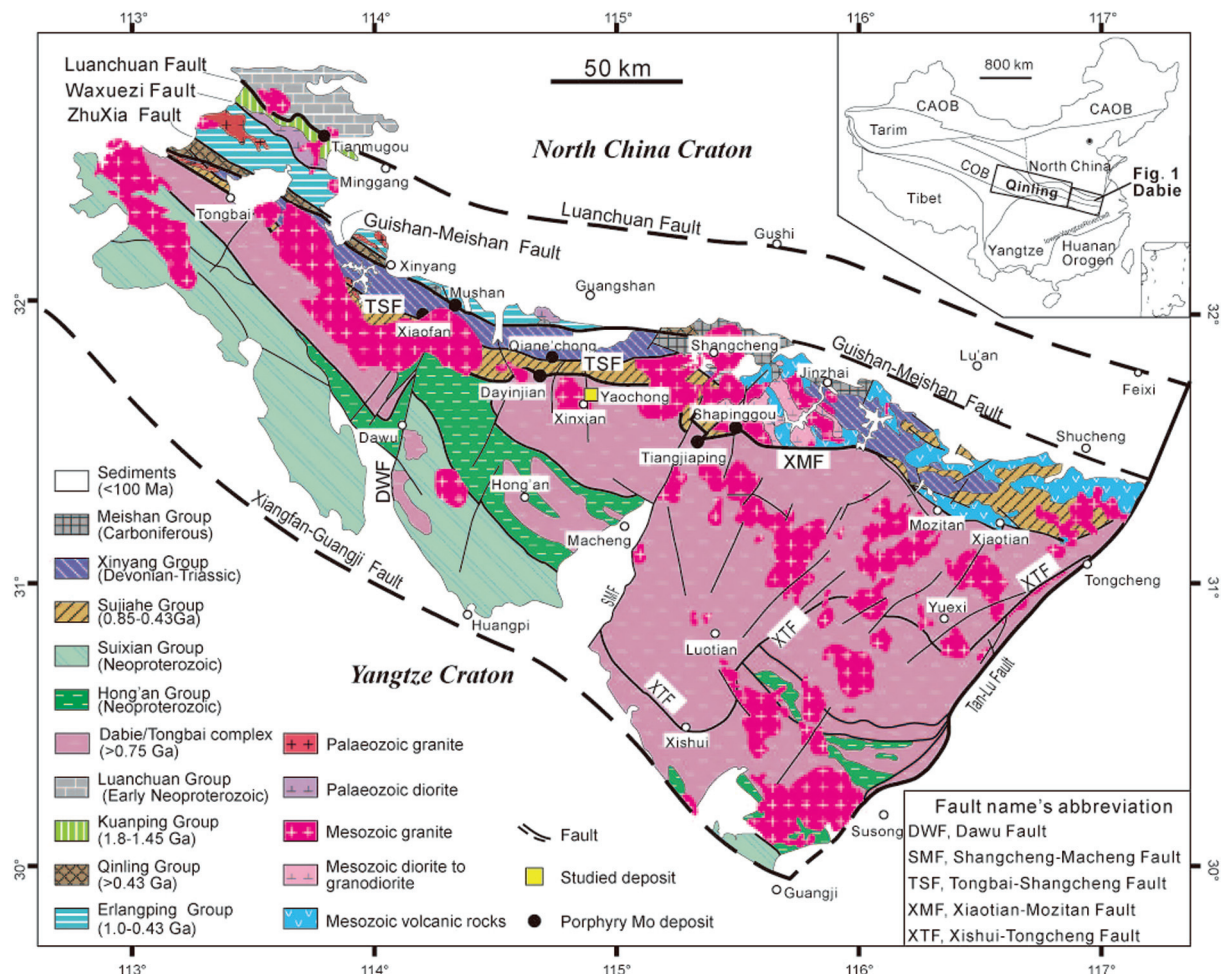


Fig. 1. Sketch map of the geology of the Dabie Mountains and the locality of the Yaochong Mo deposit (Modified after Wang et al., 2014).

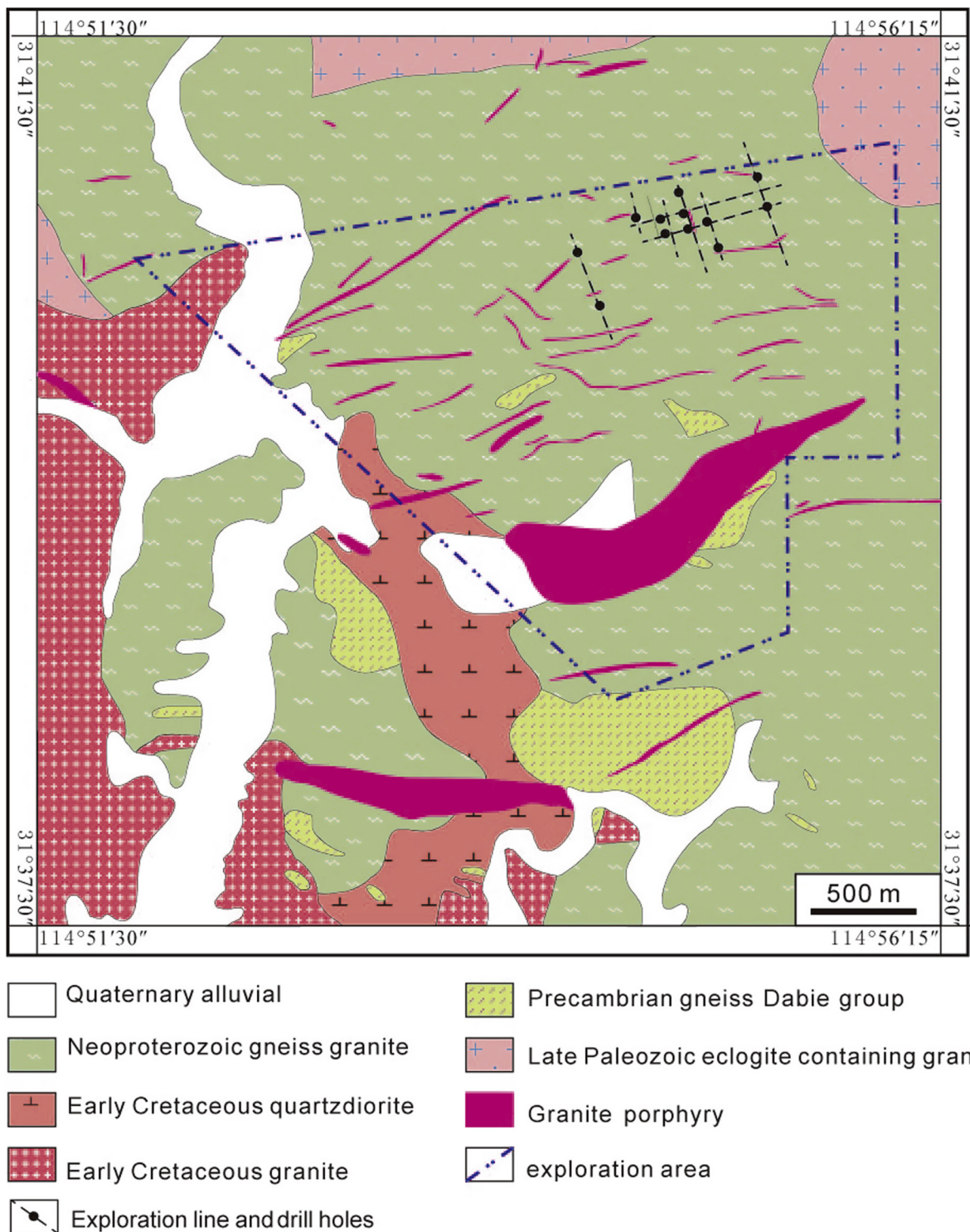


Fig. 2. Geological map of the Yaochong Mo deposit, showing the location of the exploration area and the intrusive granites (Modified by Wang et al., 2014).

molybdenite and pyrite. Minor ore minerals include chalcopyrite, magnetite, and sphalerite. The main gangue minerals include quartz and K-feldspar, with minor sericite, biotite, epidote, chlorite, and fluorite. Ore styles are disseminations, veinlets, stockworks, and breccias. The alteration assemblages at Yaochong deposit include the following: (1) potassic assemblage, which is characterized by feldspar and biotite as the predominant hydrothermal minerals and is present in the Yanshanian porphyry and wall rocks; (2) a quartz-dominated assemblage, which is

widespread in the porphyry and wall rocks, in forms of quartz blocks and quartz-sulfide stockworks; (3) a sericite-dominated assemblage, which is mainly represented by alteration of feldspar and biotite to sericite, with disseminated pyrite in veins and wall rocks; (4) propylitic assemblages, with chlorite, epidote, and calcite as predominant hydrothermal minerals; (5) carbonate-dominated assemblages, mainly characterized by carbonate veins; and (6) fluorite-bearing assemblages, mainly represented by disseminated purple fluorite grains (Wang et al., 2014).

4. Samples and analytical methods

We chose ten samples from the porphyry dikes and the buried intrusion (Fig. 3), three of them were sampled from the outcropping dikes and seven from the buried intrusion. In the exploration area that the granitic porphyry are light red, fine-grained, massive structure. The main minerals are plagioclase, K-feldspar, and quartz, the secondary minerals are epidote, biotite and metallic minerals, which are closely related to molybdenum mineralization. Due to the late tectonic events, most of the phenocrysts are fragmented. Major and trace element analyses have been carried out in the State Key Laboratory of Isotope Geochemistry, Guangzhou Institute of Geochemistry, Chinese Academy of Sciences using XRF on a Rigaku ZSX100e instrument and a Perkin-Elmer ScieX ELAN 6000 inductively coupled plasma mass spectrometer (ICP-MS), respectively. The bulk rock major elements were conducted using X-ray fluorescence spectrometry (Rigaku 100e) with analytical precisions better than 1% (Li et al., 2005). Trace elements of bulk rock samples were analyzed at the CAS Key Laboratory of Mineralogy and Metallogeny, Guangzhou Institute of Geochemistry, the Chinese Academy of Sciences, which use fluxed glasses with a sample/flux ratio of 1:3 (Liang et al., 2009). The LA-ICP-MS system consists of an Agilent 7500a ICP-MS coupled with a Resonetics RESOLution M-50 ArF-Excimer laser source ($\lambda = 193$ nm). Laser energy was 80 mJ, and frequency was 10 Hz with ablation spot of 69 μm diameter. The ablated aerosol was carried to the ICP source with He gas. NIST 612 was used as an

external calibration standard, and ^{43}Ca as the internal standard. MPI Ding-Glass was analyzed as an unknown sample to monitor (Li et al., 2012a,b; Liang et al., 2009; Tu et al., 2011). This method is the best way to analyse refractory elements, like Nb and Ta, and avoid influence from oxides.

Four samples from buried intrusion were chosen for F element analysis, they were carried out in the ALS Minerals/ALS Chemex (Guangzhou) Co Ltd, using ion electrode for F (F-ELE81a).

Zircon grains were separated from samples YC1-3, YC-6, YC-7 and YC-9, using standard density and magnetic separation techniques followed by handpicking under a binocular microscope. Selected zircon grains were mounted in epoxy mounts and then polished down to near half sections to expose internal structures. Transmitted and reflected light micrographs and cathodoluminescence (CL) images were used to identify clear domains for *in situ* analyses.

Measurements of U, Th, and Pb of zircons were carried out using a Cameca IMS 1280 large-radius SIMS at the Institute of Geology and Geophysics, CAS, Beijing. Analytical procedures are described by Li et al. (2009). The calibration of U-Th–Pb ratios was performed relative to zircon standard Plésovice (337 Ma, Sláma et al., 2008), and the correction of U concentrations was done by normalization to zircon standard 91,500 (81 ppm; Wiedenbeck et al., 1995). A long-term uncertainty of 1.5% (1RSD) for $^{206}\text{Pb}/^{238}\text{U}$ measurements of the zircon standard was propagated to the unknowns (Li et al., 2010), despite the fact that the measured $^{206}\text{Pb}/^{238}\text{U}$ error in a specific session is generally $\leq 1\%$. Zircon standard Qinghu

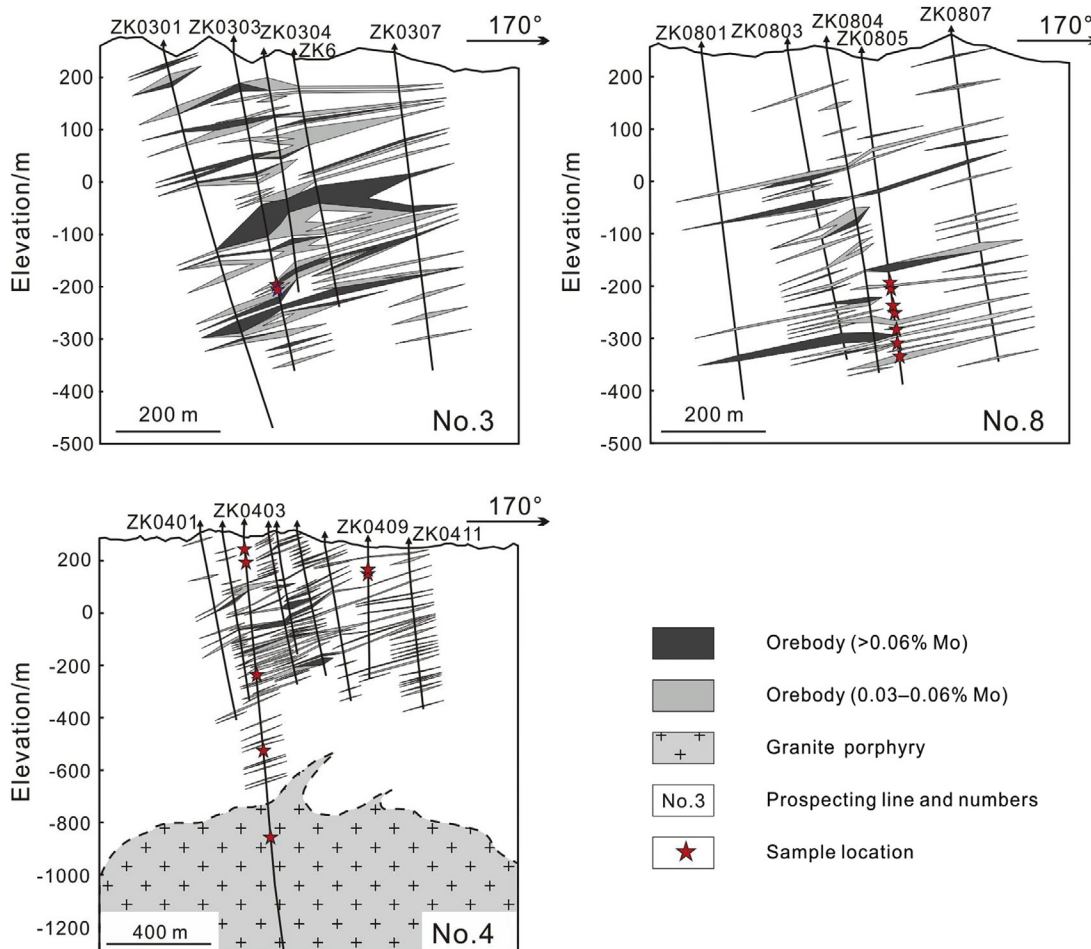


Fig. 3. Geological exploration profiles showing the location of sampled drill sites and the shape of orebody (Modified after Geological Survey Team 3 of Henan Bureau Land and Resources, 2009).

(159.5 Ma; Li et al., 2009) was alternately analyzed as an unknown sample to monitor the external uncertainties of SIMS U-Pb measurements calibrated against standard 91,500. Measured compositions were corrected for common Pb using non-radiogenic ^{204}Pb . Corrections are sufficiently small to be insensitive to the choice of common Pb composition. The average present-day crustal composition (Stacey et al., 1975) is used for the common Pb assuming that the common Pb is mainly surface contamination introduced during sample preparation. Uncertainties for individual analyses in data tables are reported at a 1σ level; mean ages for pooled U/Pb analyses are quoted at 2σ levels. Data reduction was carried out using the Isoplot/Ex v.3.0 program (Ludwig, 2003).

Trace elements analyses of zircon and apatite were carried out by LA-ICPMS at the CAS Key Laboratory of Mineralogy and Metallogeny, Guangzhou Institute of Geochemistry, CAS. A RESolution M-50 laser-ablation system was used in conjunction with an Agilent 7500 ICPMS (Li et al., 2012a,b; Liang et al., 2009; Tu et al., 2011). The clearest, least fractured rims of the zircon crystals were

selected for laser ablation analyses. Laser energy was 80 mJ and frequency was 10 Hz with ablation spot of $31\ \mu\text{m}$ in diameter. The ablated aerosol was carried to the ICP source with He and Ar gases. Both double-volume sampling cell and Squid pulse smoothing device were used to improve the data quality (Li et al., 2012a,b; Tu et al., 2011). Each spot analysis incorporated a background acquisition of approximately of 20 s, followed by 40 s sample data acquisition. Isotopes were measured in time-resolved mode. SRM NIST 610 was used as an external calibration standard, and ^{43}Ca as the internal standard to calculate the machine drift. SRM NIST 612 were tested as the monitor for quality control. The detection limits of ICP-MS for trace elements are mostly better than 10 ppb, with uncertainties of 5–10%. The calculations of trace elements were performed by ICPMSDataCal 7.0 (Liu et al., 2008). Detailed information of the methods were discussed by previous authors (Lin et al., 2016). Zircon Ce anomalies were calculated by using software from the Research School of Earth Sciences, Australian National University (Ballard et al., 2002; Liang et al., 2006).

Table 1
Major and trace element of Yaochong porphyry.

Sample	YC10-06	YC10-07	YC10-09	YC13-1	YC13-2	YC13-3	YC13-6	YC13-7	YC13-8	YC13-9
Al ₂ O ₃	15.07	14.55	14.40	14.26	14.59	16.36	14.01	15.5	13.6	14.12
CaO	0.80	0.86	1.42	1.05	1.23	0.42	1.29	2.48	0.5	1.81
Fe ₂ O ₃	1.57	1.62	1.52	1.29	1.34	1.06	2.55	3.47	0.39	2.27
K ₂ O	5.05	5.04	5.05	4.51	4.56	6.86	1.26	2.74	4.51	4.42
MgO	0.41	0.42	0.40	0.31	0.31	0.15	0.87	1.05	0.06	0.62
MnO	0.02	0.02	0.04	0.05	0.05	0.01	0.08	0.15	0.01	0.04
Na ₂ O	4.12	3.99	3.83	4.6	4.6	4.91	6.24	4.99	4.89	3.78
P ₂ O ₅	0.11	0.11	0.11	0.068	0.067	0.046	0.133	0.186	0.002	0.159
SiO ₂	71.46	71.91	71.35	71.72	71.02	68.43	71.53	66.95	74.55	69.41
TiO ₂	0.31	0.30	0.29	0.23	0.22	0.14	0.39	0.68	0.04	0.37
L.O.I	1.04	1.13	1.53	1.44	1.62	1.09	1.29	1.46	0.82	2.86
Total	99.96	99.95	99.94	99.68	99.78	99.58	99.68	99.81	99.37	100
Ti	1855	1843	1794	2300	2205	1485	3962	6869	408	3785
V	21.96	22.71	21.47	16.00	15.00	12.00	39.00	20.00	12.00	39.00
Cr	9.43	4.79	4.06	10.00	10.00	10.00	10.00	<10	<10	10.00
Mn	137	155	314	526	498	120	89	1536	118	419
Ga	22.29	21.83	21.89	26.10	27.20	37.40	15.90	20.40	38.40	20.00
Rb	169	169	171	236	237	285	38.7	103	204	160
Sr	335	328	314	273	349	208	126	309	52.2	252
Y	6.67	6.55	7.45	5.20	5.50	3.60	26.40	42.40	5.60	18.60
Zr	168	179	170	180	179	135	209	275	69	233
Nb	12.11	11.05	11.80	17.80	15.00	16.30	4.70	5.80	22.00	19.90
Cs	1.09	1.14	1.20	2.86	3.01	2.67	1.22	3.5	1.46	2.13
Ba	1699	1675	1738	1295	1285	890	411	1145	70.3	1170
La	46.6	42.5	52.0	40.3	39.2	20.2	11.2	32.1	5.4	58.6
Ce	84.1	75.5	93.9	74.1	71.6	37.1	23.4	69.8	10.3	111.5
Pr	9.26	8.48	10.47	7.52	7.42	4.03	2.94	8.61	0.97	11.55
Nd	31.6	29.3	36.3	25.5	24.4	14.8	12.5	37.1	2.6	39.7
Sm	4.60	4.30	5.21	3.48	3.35	2.26	3.15	7.87	0.41	6.25
Eu	1.11	1.06	1.26	0.67	0.75	0.57	0.94	2.43	0.09	1.17
Gd	3.14	2.95	3.62	1.72	1.71	1.54	3.57	8.07	0.42	4.10
Tb	0.31	0.31	0.37	0.20	0.19	0.14	0.60	1.20	0.06	0.63
Dy	1.23	1.22	1.43	0.77	0.87	0.71	4.00	7.20	0.39	3.27
Ho	0.19	0.19	0.22	0.13	0.14	0.12	0.94	1.57	0.12	0.60
Er	0.47	0.46	0.56	0.38	0.37	0.31	2.86	4.62	0.54	1.85
Tm	0.07	0.07	0.08	0.07	0.07	0.06	0.46	0.69	0.09	0.28
Yb	0.45	0.48	0.49	0.33	0.49	0.32	2.82	4.36	0.95	1.69
Lu	0.08	0.07	0.08	0.06	0.07	0.05	0.47	0.77	0.15	0.29
Hf	4.63	4.96	4.81	5.10	5.10	4.10	5.10	6.30	5.40	6.00
Ta	0.84	0.80	0.82	0.80	0.80	0.90	0.30	0.20	1.60	1.50
Th	12.16	11.64	11.76	18.35	16.2	15.2	5.16	3.79	27.1	25.4
U	2.66	2.936	2.76	5.19	3.93	6.2	1.06	0.81	24.6	6.22
p/al	0.0075	0.0077	0.0074	0.0048	0.0046	0.0028	0.0095	0.0120	0.0001	0.0113
k/al	0.3350	0.3465	0.3506	0.3163	0.3125	0.4193	0.0899	0.1768	0.3316	0.3130
T	791.5	795.0	783.3	787.9	785.8	758.3	799.2	813.7	713.4	807.1
Th/La	0.26	0.27	0.23	0.46	0.41	0.75	0.46	0.12	5.02	0.43
Nb/Ta	14.42	13.86	14.41	22.25	18.75	18.11	15.67	29.00	13.75	13.27
Zr/Sm	36.58	41.52	32.63	51.72	53.43	59.73	66.35	34.94	168.29	37.28
Th/U	4.57	3.96	4.26	3.54	4.12	2.45	4.87	4.68	1.10	4.08
Zr/Hf	36.33	36.00	35.37	35.29	35.10	32.93	40.98	43.65	12.78	38.83
Sr/Y	50.15	50.03	42.21	52.50	63.45	57.78	4.77	7.29	9.32	13.55
La/Yb	103.35	88.99	107.22	122.12	80.00	63.13	3.97	7.36	5.68	34.67

Table 2

Sample YC06,07,09 SIMS U-Pb ages.

Sample/	[U]	[Th]	[Pb]	Th/U	^{206}Pb	$\pm\text{s}$	^{207}Pb	$\pm\text{s}$	^{207}Pb	$\pm\text{s}$	^{206}Pb	$\pm\text{s}$	^{207}Pb	$\pm\text{s}$	^{207}Pb	$\pm\text{s}$	207-corr age (Ma)	$\pm\text{s}$
spot #	ppm	ppm	ppm	meas	^{238}U	%	^{235}U	%	^{206}Pb	%	^{238}U		^{235}U		^{206}Pb			
YC10-6@1	3874	1176	99	0.304	0.0224	2.20	0.14969	2.49	0.04848	1.17	142.8	3.1	141.6	3.3	122.8	27.3	142.8	3.1
YC10-6@2	464	117	11	0.253	0.0215	2.23	0.14939	3.27	0.05039	2.39	137.1	3.0	141.4	4.3	213.0	54.4	136.9	3.0
YC10-6@3	2185	558	51	0.255	0.0211	2.20	0.14029	5.01	0.04811	4.50	134.9	2.9	133.3	6.3	104.8	102.9	135.0	3.0
YC10-6@4	440	81	10	0.184	0.0210	2.22	0.14003	3.34	0.04833	2.50	134.0	3.0	133.1	4.2	115.6	57.8	134.1	3.0
YC10-6@5	306	604	11	1.971	0.0218	2.22	0.14017	5.99	0.04654	5.56	139.3	3.1	133.2	7.5	25.5	128.3	139.7	3.1
YC10-6@6	358	564	11	1.576	0.0204	2.24	0.13815	3.70	0.04912	2.94	130.2	2.9	131.4	4.6	153.3	67.4	130.1	2.9
YC10-6@7	2428	436	57	0.179	0.0213	2.20	0.14401	2.65	0.04895	1.47	136.1	3.0	136.6	3.4	145.6	34.1	136.1	3.0
YC10-6@8	379	365	10	0.964	0.0205	2.28	0.14547	3.80	0.05135	3.05	131.1	3.0	137.9	4.9	256.5	68.5	130.7	3.0
YC10-6@9	831	121	20	0.146	0.0219	2.20	0.14790	3.01	0.04887	2.06	140.0	3.0	140.1	3.9	141.8	47.6	139.9	3.1
YC10-6@10	1343	900	36	0.670	0.0218	2.20	0.15124	2.96	0.05029	1.97	139.1	3.0	143.0	3.9	208.6	45.0	138.8	3.0
YC10-6@11	779	151	18	0.193	0.0210	2.29	0.13932	3.27	0.04817	2.34	133.8	3.0	132.4	4.1	107.4	54.3	133.9	3.0
YC10-6@12	1896	406	44	0.214	0.0211	2.21	0.13747	2.90	0.04722	1.88	134.7	2.9	130.8	3.6	60.1	44.2	135.0	3.0
YC10-6@13	1357	869	34	0.640	0.0206	2.22	0.13294	3.87	0.04688	3.17	131.2	2.9	126.7	4.6	43.1	74.1	131.5	2.9
YC10-7@1	5556	2271	140	0.409	0.0217	2.27	0.14503	2.60	0.04858	1.27	138.1	3.1	137.5	3.3	127.6	29.6	138.1	3.1
YC10-7@2	1372	1115	38	0.392	0.0214	2.20	0.14103	3.28	0.04776	2.43	136.6	3.0	134.0	4.1	87.2	56.6	136.8	3.0
YC10-7@3	1090	319	26	0.812	0.0210	2.21	0.14151	2.93	0.04889	1.93	133.9	2.9	134.4	3.7	142.6	44.7	133.9	2.9
YC10-7@4	1485	378	35	0.292	0.0210	2.25	0.13911	2.90	0.04797	1.83	134.2	3.0	132.3	3.6	97.7	42.8	134.3	3.0
YC10-7@5	876	344	21	0.254	0.0209	2.28	0.13817	3.30	0.04793	2.38	133.4	3.0	131.4	4.1	95.8	55.5	133.5	3.0
YC10-7@6	685	254	17	3.972	0.0213	1.61	0.14396	3.34	0.04907	2.93	135.7	2.2	136.6	4.3	151.2	67.2	135.7	2.2
YC10-7@7	1296	1291	38	0.323	0.0210	1.51	0.14196	2.50	0.04894	1.99	134.2	2.0	134.8	3.2	144.9	46.1	134.2	2.0
YC10-7@8	2225	8837	103	0.443	0.0218	1.54	0.13948	3.00	0.04649	2.58	138.8	2.1	132.6	3.7	23.0	60.7	139.2	2.1
YC10-7@9	1993	643	50	0.786	0.0221	1.53	0.14891	2.15	0.04885	1.50	141.0	2.1	140.9	2.8	140.8	34.9	141.0	2.2
YC10-7@10	2215	980	56	0.370	0.0216	1.56	0.14479	2.07	0.04856	1.36	137.9	2.1	137.3	2.7	126.7	31.8	137.9	2.1
YC10-7@11	2453	1929	66	0.996	0.0218	1.51	0.13473	6.93	0.04481	6.77	139.1	2.1	128.3	8.4	-65.8	157.5	139.7	2.4
YC10-7@12	895	338	22	0.378	0.0216	2.11	0.14354	2.99	0.04823	2.11	137.7	2.9	136.2	3.8	110.4	49.1	137.8	2.9
YC1-3 U-Pb ICP-MS age																		
Pb	Th	U	Th/U	$^{207}\text{Pb}/^{206}\text{Pb}$		$^{207}\text{Pb}/^{235}\text{U}$		$^{206}\text{Pb}/^{238}\text{U}$		$^{207}\text{Pb}/^{206}\text{Pb}$		$^{207}\text{Pb}/^{235}\text{U}$		$^{206}\text{Pb}/^{238}\text{U}$		$^{208}\text{Pb}/^{232}\text{Th}$		
ppm	ppm	ppm	calc	Ratio	1 σ	Ratio	1 σ	Ratio	1 σ	Age (Ma)	1 σ	Age (Ma)	1 σ	Age (Ma)	1 σ	Age (Ma)	1 σ	

1	10	214	358	0.598	0.0398	0.0094	0.1133	0.0289	0.0214	0.0004	error	109	26.3	136.6	2.5	129.9	5.4	
2	10	220	316	0.696	0.0382	0.0076	0.1225	0.0257	0.0235	0.0004	error	117.3	23.3	149.8	2.6	148.9	5.9	
3	3	134	88	1.515	0.0728	0.0119	0.1986	0.0325	0.0202	0.0005	1009.3	335.2	183.9	27.5	129.1	3.5	135.8	6.3
4	11	335	383	0.874	0.0382	0.0044	0.1154	0.0129	0.0214	0.0003	error	110.9	11.8	136.5	2.2	138	4.8	
5	5	136	173	0.785	0.0492	0.0059	0.147	0.0169	0.0213	0.0004	166.75	245.0	139.2	14.9	136.1	2.8	143.5	6.1
6	7	123	251	0.488	0.0539	0.0051	0.1713	0.0145	0.0232	0.0005	364.9	212.9	160.5	12.6	147.6	3.2	153.8	6.9
7	18	400	644	0.621	0.0522	0.0045	0.1679	0.0149	0.0224	0.0004	294.5	198.1	157.6	12.9	142.8	2.6	174	10.2
8	4	167	141	1.191	0.0577	0.0053	0.1601	0.0149	0.0201	0.0005	520.4	203.7	150.8	13	128.2	3	131.5	5.3
9	6	165	217	0.761	0.057	0.0041	0.1767	0.0129	0.0223	0.0004	494.5	165.7	165.2	11.1	141.9	2.7	144	6.5
10	37	677	1369	0.494	0.0442	0.0018	0.1412	0.0059	0.0228	0.0003	error	134.1	5.2	145.2	2.1	146.1	4.9	
11	23	743	819	0.908	0.0491	0.0022	0.1434	0.0063	0.021	0.0003	153.8	107.4	136	5.6	134	2.1	129.9	4.2
12	110	2661	3887	0.685	0.0469	0.0015	0.1445	0.0049	0.0219	0.0003	55.7	64.8	137	4.4	139.9	1.9	135.8	4.4
13	8	228	279	0.818	0.0506	0.0033	0.1486	0.0092	0.0216	0.0004	220.4	150.0	140.7	8.1	137.9	2.7	132.2	5.7
14	18	499	637	0.783	0.0476	0.0027	0.1498	0.009	0.0225	0.0004	76.0	129.6	141.7	7.9	143.7	2.7	138.2	5.5
15	9	229	332	0.691	0.046	0.003	0.1407	0.0098	0.0222	0.0004	error	133.6	8.7	141.5	2.4	138.8	5.8	
16	9	176	290	0.606	0.0608	0.0041	0.1861	0.0119	0.0227	0.0005	631.5	145.2	173.3	10.2	144.7	3	175.2	7.8
17	5	137	154	0.89	0.0795	0.0057	0.2244	0.0158	0.0208	0.0004	1183.3	142.6	205.6	13.1	132.8	2.6	160.5	7.5
18	7	156	249	0.628	0.0713	0.0047	0.1899	0.012	0.0195	0.0003	964.8	131.02	176.5	10.3	124.7	2.1	168.7	7.7

Fluorine and chlorine compositions of apatite from the Yaochong porphyry intrusions and dykes were determined by a JXA-8100 electron microprobe at the Key Laboratory of Submarine Geosciences, State Oceanic Administration, Second Institute of Oceanography, SOA, Hangzhou. The analyzing conditions were 15 keV and 20 nA current, with a 10 μm diameter electron beam. Norbergite was used

as standard for F, and $\text{Ba}_5(\text{PO}_4)_3\text{Cl}$ for Cl, apatite for Ca and P standards. Counting times were 20 s for Si, Al, Mg, Fe, Mn, Ca, Sr, and P and reduce to 10 s for F and Cl to avoid volatile loss. Fluorine was determined using K α line obtained with a LDE1 crystal and chlorine was determined using K α line obtained with a PET crystal. Detail method was described previously (Li et al., 2012a,b).

Table 3
Fluorine content of the Yaochong samples.

Sample Description	F ppm
Yc-4	2080
Yc-5	2210
Yc-6	1800
Yc-7	1480
Yc-9	1670

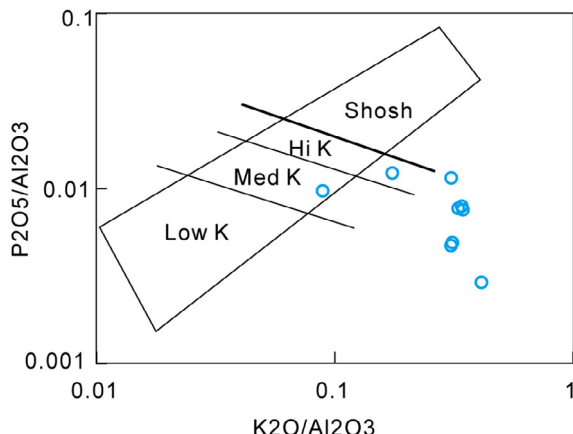


Fig. 4. Diagrams of P_2O_5/Al_2O_3 vs. K_2O/Al_2O_3 , showing that the Yaochong porphyry falls into the High K and Med K area. Modified after (Crawford et al., 2007).

5. Results

5.1. Whole-rock major and trace elements

Ten samples were analyzed for major and trace element compositions. The Yaochong granite is characterized by higher SiO_2 (66.9–74.5 wt%), Al_2O_3 (13.6–16.3 wt%), Fe_2O_3 (0.39–3.47 wt%), Na_2O (3.78–6.24 wt%), K_2O (1.26–6.86 wt%) contents, and lower TiO_2 (0.04–0.68 wt%), MgO (0.06–0.87 wt%), CaO (0.5–2.48 wt%), and P_2O_5 (0.01–0.19 wt%). Almost all the granites formed at temperature of 758–817 °C (Table 1).

Trace elements of the samples are characterized by high concentrations of large ion lithophile elements (LILE). According to the chondrite-normalized REE diagram, they are enriched in light rare earth elements (LREE) relative to heavy rare earth elements (HREE) and show negative Eu-anomalies, which indicates removal of plagioclase by fractional crystallization during magma evolution.

5.2. Whole rock F contents

Four samples were selected for the F content analysis, the fluorine concentrations of the whole rock varying from 1480 to 2210 ppm (Table 3), lower than the Climax-type Mo deposit (commonly >1 percent).

5.3. Zircon U-Pb age and trace element

Zircon U-Pb dating was conducted on four samples. Three of them (YC10-06, YC10-07 and YC10-09) were determined by SIMS.

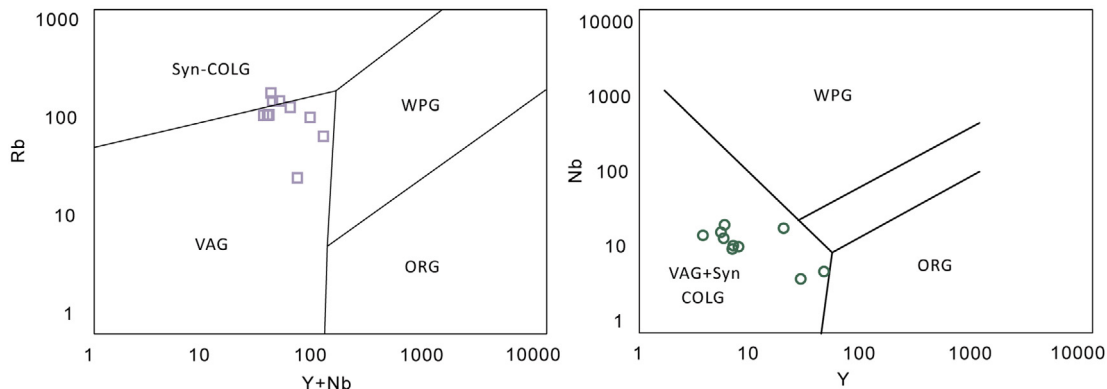


Fig. 5. Tectonic discrimination diagram (Pearce et al., 1984). The Yaochong granites are plotted in the field of VAG + Syn COLG.

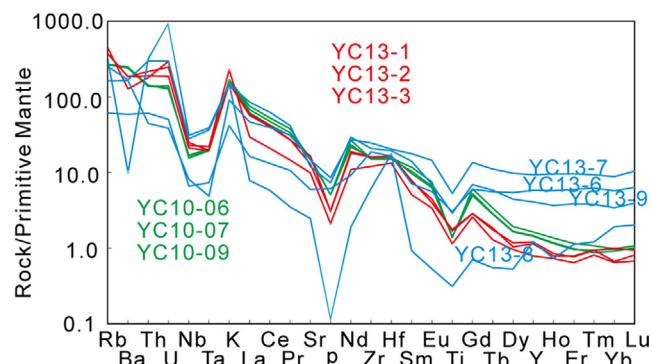
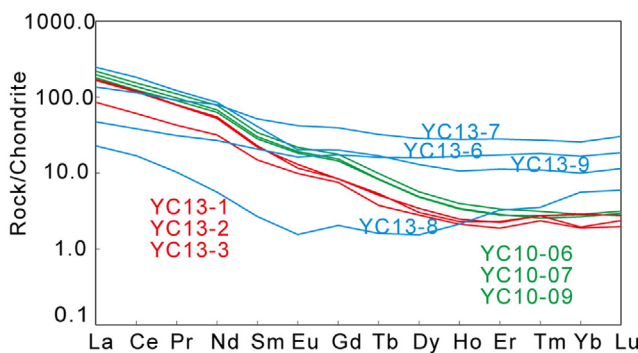


Fig. 6. (a) Chondrite-normalized rare earth element (REE) patterns for the Yaochong magmatic rocks. (b) Primitive mantle-normalized rare earth element (REE) patterns for the Yaochong magmatic rocks. Primitive mantle normalizing values are from Sun and McDonough (1989).

The other one (sample YC13-1) was determined by LA-ICP-MS. Zircon U-Pb dating results are listed in Table 2.

CL images of the zircon from sample YC13-1 display tight oscillatory zoning, which is typical of granitic zircons, consistent with high Th/U (0.5–1.0), zircons from other samples with slightly

hydrothermal alteration features, with a wide range Th/U (0.2–1.9) (Fig. 8). SIMS zircon U-Pb dating for sample YC10-6 yields $^{206}\text{Pb}/^{238}\text{U}$ age 135.4 ± 2.3 Ma, sample YC10-7 yields $^{206}\text{Pb}/^{238}\text{U}$ age 136.9 ± 1.6 Ma and sample YC10-9 yields $^{206}\text{Pb}/^{238}\text{U}$ age 134.9 ± 1.9 Ma (Fig. 7). LA-ICP-MS analysis for zircons from sample

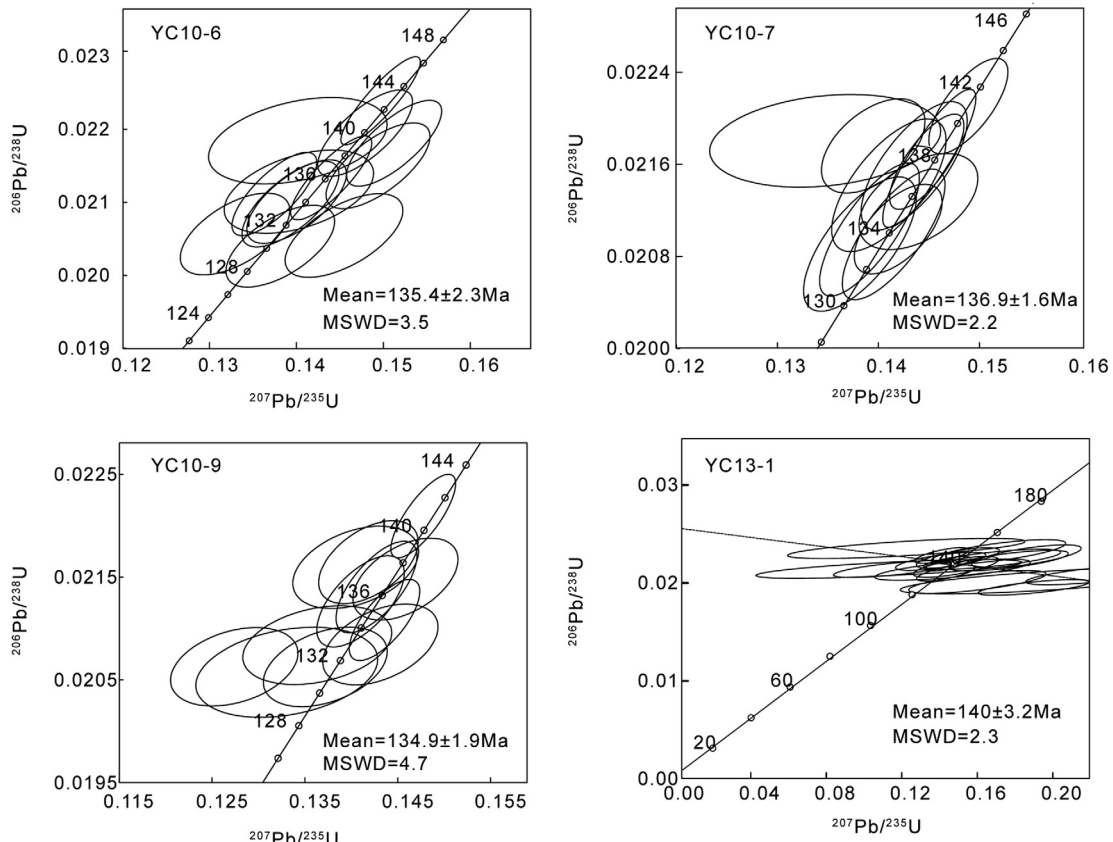


Fig. 7. U-Pb concordia diagram showing analytical results for zircons and the weighted average $^{206}\text{Pb}/^{238}\text{U}$ ages about 134.9–136.9 Ma for analyses of Yaochong 6, 7, 9 (A, B, C); 140 ± 3.2 Ma for analyses of Yaochong 1–3 (D). Data for the Yaochong porphyry ages are listed in Table 2.

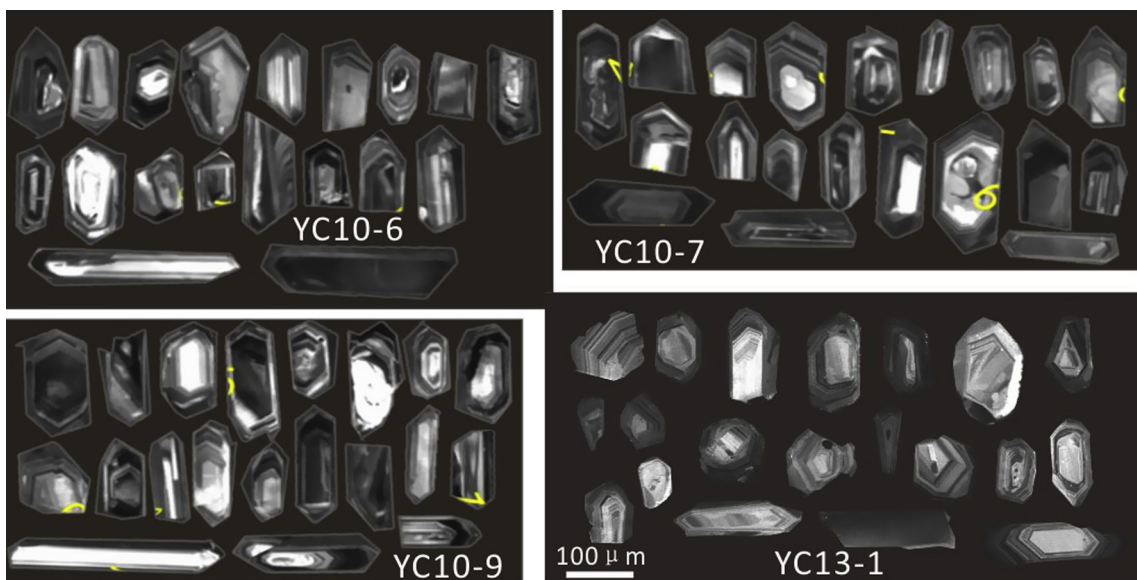


Fig. 8. Cathodoluminescence (CL) images of mineralized porphyry samples from the Yaochong porphyry intrusions, showing the magmatic and hydrothermal zircons.

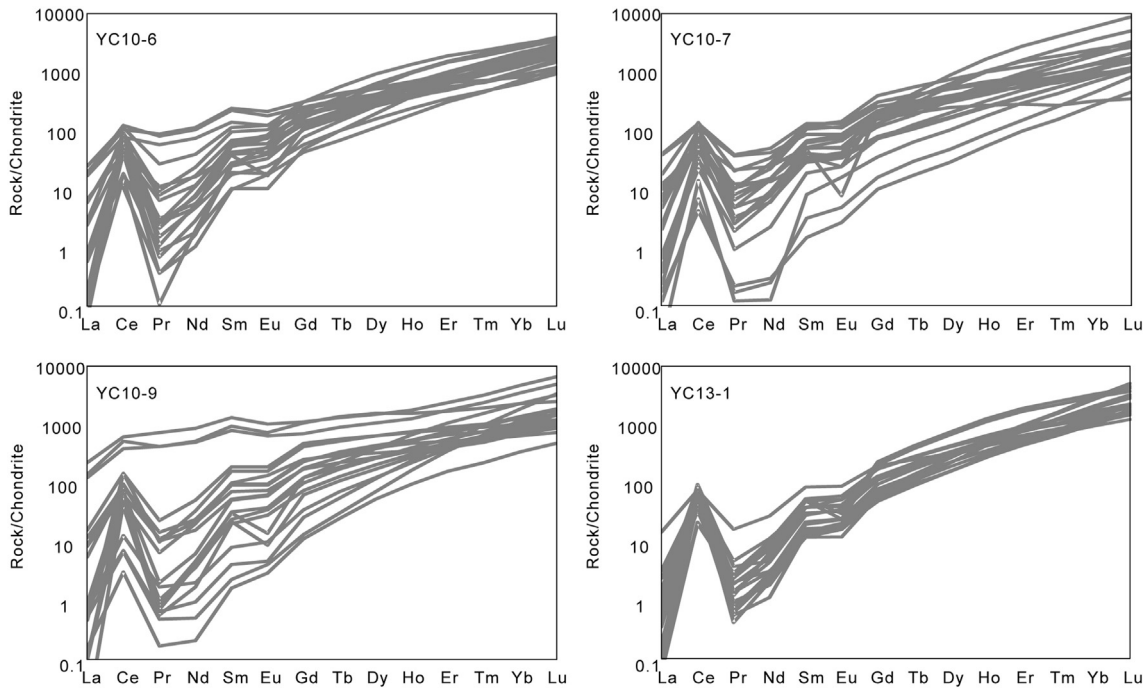


Fig. 9. Zircon chondrite-normalized REE diagram. Chondritic values are from Sun and McDonough (1989).

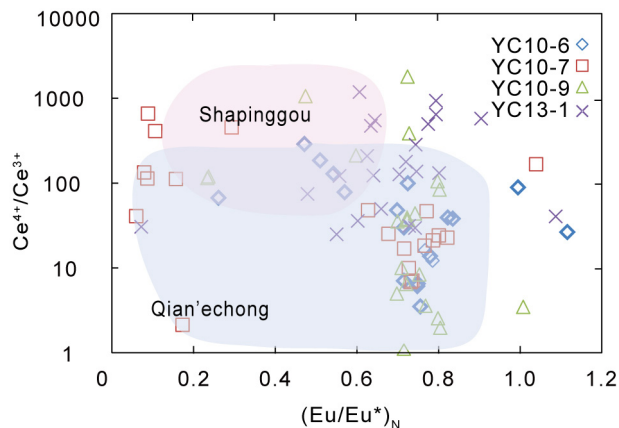


Fig. 10. $\text{Ce}^{4+}/\text{Ce}^{3+}$ and $(\text{Eu}/\text{Eu}^*)_N$ ratios of individual grains for Yaochong porphyry deposits as well as Qian'echong and Shapinggou porphyries from Dabie, China. Data of Qian'echong and Shapinggou samples in Dabie were all from the buried intrusions and the dykes (Mi et al., 2014; Zhang et al., 2015). This diagram shows that the Yaochong porphyry has more varied oxygen fugacity.

YC13-1 yields $^{206}\text{Pb}/^{238}\text{U}$ age 140 ± 3.2 Ma (Fig. 7). The dating results suggest that the altered dikes were formed ~ 5 Ma earlier than the buried intrusions.

These zircon grains are LREE depleted and HREE enriched, with Ce concentrations ranging from 2 to 385 ppm, and Eu concentrations ranging from 0.2 to 60 ppm. These grains are characterized by positive Ce and negative Eu anomalies. The zircon grains from sample YC10-6, YC10-7 and YC10-9 show larger range of LREE concentrations (Fig. 9), whereas sample YC13-1 shows a complete accord of REE patterns (Fig. 9). Zircon grains from YC samples have $\text{Ce}(\text{IV})/\text{Ce}(\text{III})$ and $(\text{Eu}/\text{Eu}^*)_N$ ratios ranging from 2 to 1800 and from 0.1 to 1.1, respectively (Appendix I). These highly varied ratios show that the zircons were not from the unique source.

Use Ti-in-zircon thermometer, the temperature of zircon formation ranges from 650–750 °C (Appendix I). This is relatively lower than the Qian'echong 700–740 °C (Mi et al., 2015b) and

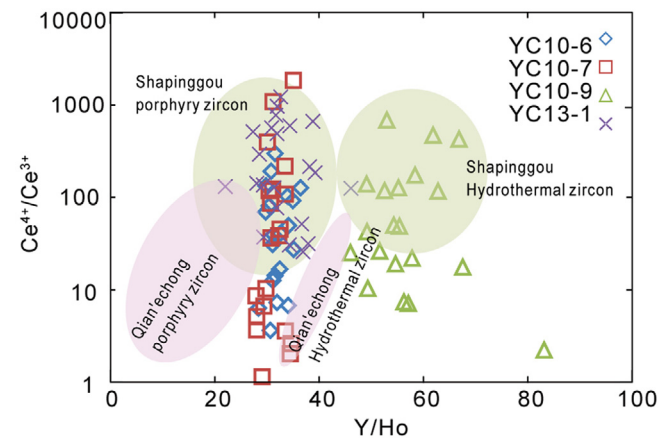


Fig. 11. $\text{Ce}^{4+}/\text{Ce}^{3+}$ and Y/Ho ratios of individual grains for Yaochong porphyry deposits as well as Qian'echong and Shapinggou porphyries from Dabie, China. Data of Qian'echong and Shapinggou samples in Dabie were all from the buried intrusions and the dykes (Mi et al., 2015a; Zhang et al., 2014).

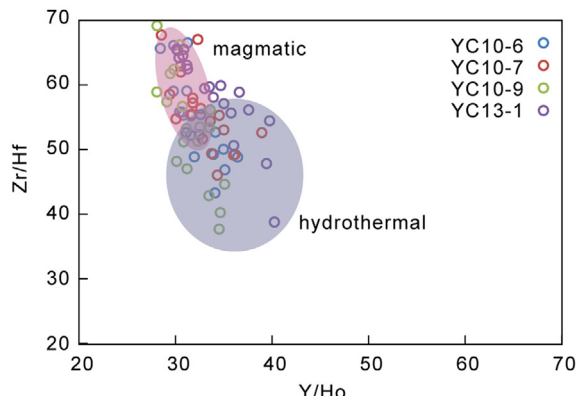


Fig. 12. Zr/Hf and Y/Ho ratios of individual grains for Yaochong porphyry deposits, pink oval-shaped area showing the magmatic zircon and the blue oval-shaped area showing the hydrothermal zircons (Bau, 1996).

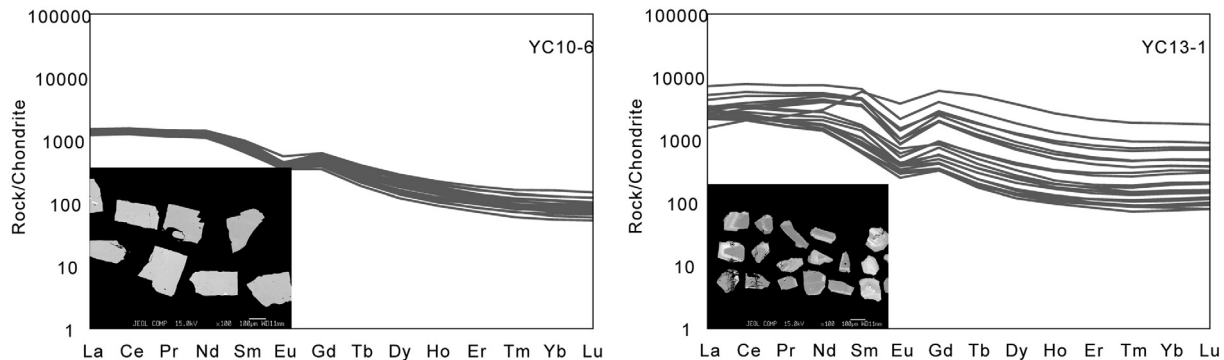


Fig. 13. Backscattered electron (BSE) images of apatite from Yaochong porphyries, Apatite chondrite-normalized REE diagram. Chondritic values are from Sun and McDonough (1989). (A) Apatite grains from sample YC10-6 are all intact prismatic crystals and have smooth surface, they had accordant REE diagram; (B) Apatite grains from sample YC13-1 have difference of the surface characteristics may caused by slight discrepancy of minerals composition.

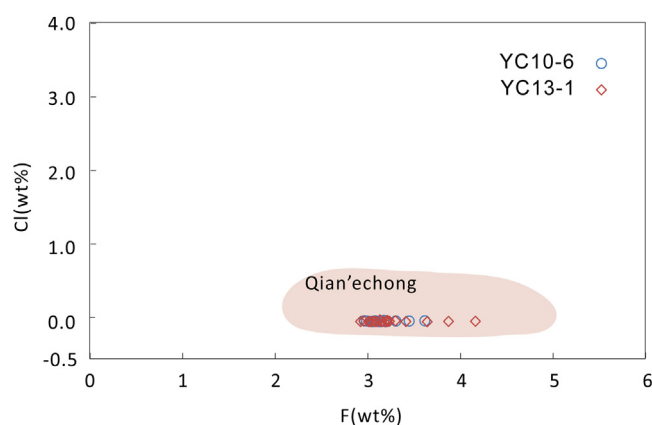


Fig. 14. A diagram of F versus Cl in apatite from Yaochong deposit. (A) The colored dots represents Yaochong Mo porphyry deposit; (B) The lavender area represents Dexing copper porphyry deposit (Zhang et al., 2013), the pale blue area represents Qian'echong porphyry deposit (Mi et al., 2015b). Compared to the Dexing apatite, the Yaochong apatite has higher F but lower Cl concentrations, similar to Qian'echong apatite.

Shapiggou 820–860 °C (Zhang et al., 2013). These represent the temperatures at which zircon crystallized. The magmas may have experienced slightly higher temperatures.

5.4. Apatite major and trace elements

The apatite grains from sample YC10-6 are mostly intact prismatic crystals and have smooth surface as shown by backscattered electron (BSE) images (Fig. 13). The grains from sample YC13-1 have fractures and corrossions surface (Fig. 13). The fluorine concentrations in apatite grains are relative high, varying from 2.9% to 4.1%. In contrast, the chorine concentrations in apatite are very low, ranging from 0.001% to 0.010% (Appendix II). The ratios of fluorine and chorine are extremely high, indicating that these studied apatite grains here all belong to fluorapatite Figs. 14 and 15.

The chondrite-normalized REE patterns of apatite from the Yaochong porphyries are enriched in LREE and depleted in HREE, with negative Eu anomalies (Appendix III). The apatite grains of outcrop sample YC10-6 show similar patterns for those with smooth surface and those without fractions and zones. The apatite grains of the buried porphyry sample YC13-1 show more scattered patterns, with fractures and diversity zones on the surface (Fig. 13). These differences between sample YC10-6 and YC13-1 indicating that the YC13-1 experienced more fluid influences.

6. Discussion

6.1. Oxidation state and rock-forming temperatures

Zircon is a good record of oxygen fugacity (Ballard et al., 2002; Liang et al., 2006). Magmatic zircon usually has a positive Ce anomaly, depending on the oxygen fugacity. Ce^{4+} is much more compatible in zircon than Ce^{3+} , zircon crystallized from magma with a higher oxygen fugacity has a larger Ce anomaly. The $\text{Ce}^{4+}/\text{Ce}^{3+}$ value is a sensitive and robust indicator of magmatic oxidation state given that zircon is very refractory (Ballard et al., 2002). In addition, the ionic radii of Eu^{3+} are smaller than those of Eu^{2+} , and Eu^{3+} is preferentially incorporated into zircon over Eu^{2+} . Therefore, Eu anomalies may also reflect oxygen fugacities.

The calculated $\text{Ce}^{4+}/\text{Ce}^{3+}$ values of the Yaochong zircon are variable from 2 to 1940, the intrusion has slightly higher Ce anomalies than the outcrop porphyry veins. In a $\text{Ce}^{4+}/\text{Ce}^{3+}$ versus $(\text{Eu}/\text{Eu}^*)_{\text{N}}$ diagram, most Yaochong samples fall in the upper right area, suggesting high oxygen fugacity of the Yaochong porphyry. The large range of the values shows that the Yaochong porphyry dykes and intrusions have complicated evolution (Figs. 10, 11, 12).

Zircon is much more resistant to alteration than most rock-forming minerals and has high closure temperatures, even >900 °C for U-Pb system (Lee et al., 1997). It is a good record of oxygen fugacity (Ballard et al., 2002; Bolhar et al., 2008; Li et al., 2012a,b; Liang et al., 2006) and a reliable geothermometer, which is stable through high-grade metamorphism and partial melting of the host rock (Lee et al., 1997). Using the Ti-in-zircon thermometer, the magmatic zircon grains yield temperatures of 675–713 °C, with slightly higher temperatures for the porphyry veins than the buried intrusions. These temperatures are similar to, but slightly lower than that of the Qian'echong porphyries (Mi et al., 2015b) but much lower than that of Shapiggou Mo deposit with porphyry (860 ± 30 °C) (Zhang et al., 2013).

6.2. Yaochong, a Low-F stockwork Mo deposit in the Dabie Mountains

Climax-type porphyry Mo deposits are mostly distributed in western North America. They are consistently found in a post-subduction, extensional tectonic setting and are associated with A-type granites. Low-fluorine stockwork molybdenite deposits are closely related to subduction related magmas, similar to porphyry copper deposits, e.g., being similar in their tectonic setting and the petrology (calc-alkaline) of associated igneous rock types. In the eastern Pacific, low-F porphyry Mo deposits are mainly restricted to the western Canada and the northwest United States.

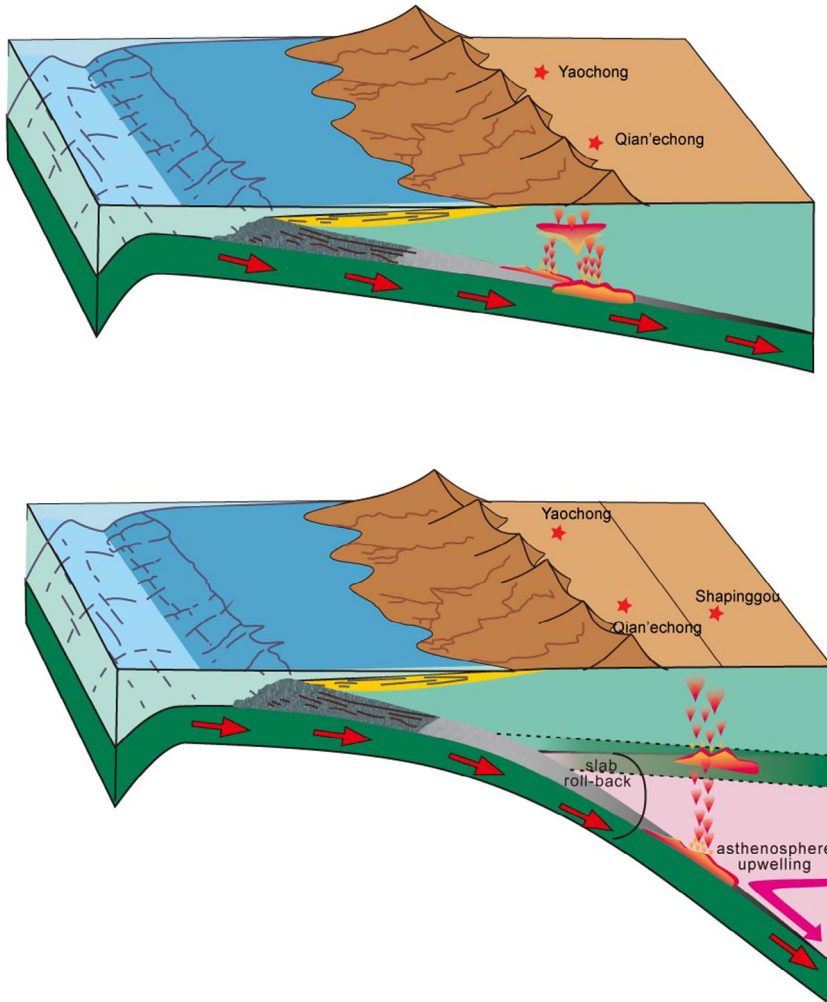


Fig. 15. The Pacific plate was subducting towards the Yangtze Block, with the ridge between Pacific and Izanagi plates pointing towards the Qinling orogenic belt at ~140 Ma (Sun et al., 2007, 2010; Ling et al., 2009). The front of the subducting plate may have reached the Dabie Mountains (Ling et al., 2011), resulting in adakites (Wang et al., 2007; Huang et al., 2008; He et al., 2011). The Yaochong Low-F Mo deposits was located near the front edge of the subducting plate. During slab roll-back commenced at ~115 Ma, Climax-type Shapinggou Mo deposit associated with A-type granite formed. Therefore, the front line of the subducting plate was likely between Yaochong and Shapinggou.

The Yaochong Mo porphyry deposit is similar in many ways to the Low-F stockwork deposits in the USA (Ludington et al., 2009b). First, in mining grade and associated mineralization, Yaochong is a Mo deposit with Mo content 0.058% and with economic concentrations of Cu. Second, petrological characteristic showing that Yaochong porphyry belongs to middle to high K series (Fig. 4), which is different from the A-type granites Climax deposits. Moreover, the Yaochong porphyry has low Rb (39–285 ppm), Nb (5–22 ppm) and Ta (0.2–1.6 ppm), and high Sr (52–334 ppm), which are also different from those of the Climax deposits (Table 1) (Carten et al., 1988). In addition, F content is another characteristic of the Low-F type deposits. Yaochong Mo deposit has fluorine contents of 1670–2210 ppm. In contrast, plutons enriched in fluorine (commonly have >1 percent) in Climax deposits. They are also in common with the ore-forming fluid system, types of vein and the compositional types of fluid inclusion (pure CO₂, CO₂ bearing, aqueous, and solid bearing). The ore-forming fluid system at Yaochong was initially high temperature, high salinity, and CO₂-rich and then progressively evolved to CO₂-poor, lower salinity, and lower temperature, by mixing with meteoric water, which results in ore precipitation. Yaochong was initially high temperature (128–501 °C), high salinity (<13 wt% NaCl eq.), the H-O-C isotope result (quartz separates from the veins yielded a δ¹⁸O value of 7.7–11.2‰, corresponding to δ¹⁸O_{H2O} values of −1.3 to 6.9‰ using

temperature estimates from fluid inclusion data; δD_{H2O} values of fluid inclusion vary from −80 to −55‰, and δ¹³C_{CO2} from −2.3 to 2.7‰) suggesting that the ore-fluids evolved from magmatic to meteoric sources (Wang et al., 2014), which is also consistent with low-F type deposits Figs. 5 and 6.

6.3. Tectonic setting of Yaochong porphyry Mo deposit

The Qinling orogenic belt has experienced two major collisions: a Palaeozoic collision along the Shangdan suture and a Triassic collision along the Mianlue-Huwan suture (Sun et al., 2002a,b; Meng and Zhang, 1999, 2000; Qin et al., 2008, 2009, 2010). In the Triassic, the South and North China Blocks finally collided, forming the famous Dabie-Sulu ultrahigh-pressure metamorphic belt in the east (Hacker et al., 1998; Zheng et al., 2003; Li et al., 1993) as well as syn-orogenic granites in the Qinling region in the west section of the Qinling-Dabie orogenic belt (Sun et al., 2002a; Qin et al., 2007; Zhou et al., 2008). Most of the Mo mineralization in the Qinling-Dabie orogen however occurred in the Cretaceous (Li et al., 2003, 2004, 2005, 2006, 2012a,b; Lu et al., 2002; Mao et al., 2005, 2008, 2010; Zhu et al., 2008; Wang et al., 2017). There are two mineralization events in the Qinling orogen in the Early Cretaceous, the main Mo mineralization occurred between 130 and 148 Ma and the later one at ~115 Ma (Li et al., 2012a,b).

Yaochong was formed at 134–140 Ma, belongs to the first peak in the Early Cretaceous period ~145 Ma (total tonnage >3.5 Mt). Previous authors proposed that this peak age of the Qinling molybdenum belt approximates to that of adakitic rocks and corresponding Cu-Au deposits in the lower Yangtze River belt (Li et al., 2012a, b). In addition, the linearly distributed Lower Yangtze River belt is roughly the east extension of the Qinling molybdenum belt. The magmatic and mineralization event in the lower Yangtze River belt has been attributed to a ridge subduction, based on the drifting history of the Pacific plate, as well as the distribution of adakites, A-type granites, and associated deposits (Ling et al., 2009; Sun et al., 2010). This is supported by geochemical studies (Liu et al., 2010; Ling et al., 2011). Given that ridge subduction may cause deformation in the overriding plate far away from the subduction zone (Espurt et al., 2008; Sobolev and Yu Babeyko, 2005), it is likely that the magmatism and mineralization in Qinling molybdenum belt were triggered by the ridge subduction along the lower Yangtze River belt, which caused reactivation of the Qinling orogenic belt along the Erlangping back-arc basin due to the far-field effect of the ridge subduction. During the magmatism, Mo-enriched back-arc meta-sediments were involved, resulting in high-Mo primitive magmas and Mo deposits.

7. Conclusions

The Yaochong intrusion formed at about 140 Ma. This belongs to the main mineralization period in the Qinling-Dabie Mo belt. The large range of the oxygen fugacity values and the temperature indicate that the Yaochong porphyry dykes and intrusions have a more complex evolution history.

The Yaochong deposit is similar to the low-F Mo deposit in terms of geochemical characteristics and tectonic settings. Based on the tectonic evolution in eastern China, we propose that the Yaochong Mo deposit formed by a far-field effect of the ridge subduction along the Lower Yangtze River Belt.

Acknowledgments

This work is supported by the DREAM project of MOST China (2016YFC0600408), NSFC (No 41203029, 41403034, 41421062) and Ministry of Land and Resources Non-profit sector research special project (201111007-1). The field investigation was supported by Geological Team 3 of the Henan Bureau of Land and Resources, Henan Province Academy of Land and resources. This is contribution No. IS-2380 from GIGCAS.

Appendix A. Supplementary data

Supplementary data associated with this article can be found, in the online version, at <http://dx.doi.org/10.1016/j.oregeorev.2017.03.029>.

References

- Ballard, J.R., Palin, M.J., Campbell, I.H., 2002. Relative oxidation states of magmas inferred from Ce(IV)/Ce(III) in zircon: application to porphyry copper deposits of northern Chile. *Contrib. Miner. Petrol.* 144, 347–364.
- Bau, M., 1996. Controls on the fractionation of isovalent trace elements in magmatic and aqueous systems: evidence from Y/Ho, Zr/Hf, and lanthanide tetrad effect. *Contrib. Miner. Petrol.* 123, 323–333.
- Bolhar, R., Weaver, S.D., Palin, J.M., Cole, J.W., Paterson, L.A., 2008. Systematics of zircon crystallisation in the Cretaceous Separation Point Suite, New Zealand, using U/Pb isotopes, REE and Ti geothermometry. *Contrib. Miner. Petrol.* 156, 133–160.
- Carten, R.B., Geraghty, E.P., Walker, B.M., Shannon, James R., 1988. Cyclic development of igneous features and their relationship to high-temperature hydrothermal features in the Henderson porphyry molybdenum deposit, Colorado. *Econ. Geol.* 83 (2), 266–296.
- Carten, R.B., White, W.H., Stein, H.J., 1993. High-grade granite-related molybdenum systems: classification and origin. *Mineral deposit modeling: Geological Association of Canada Special Paper* 40, 521–554.
- Crawford, A.J., Meffre, S., Squire, R.J., Barron, L.M., Falloon, T.J., 2007. Middle and Late Ordovician magmatic evolution of the Macquarie Arc, Lachlan Orogen, New South Wales. *Aust. J. Earth Sci.* 54, 181–214.
- Chen, Y.J., Wang, P., Li, N., Yang, Y.F., Pirajno, F., 2017. The collision-type porphyry Mo deposits in Dabie Shan, China. *Ore Geol. Rev.* 81 (2), 405–430.
- Espurt, N., Funiciello, F., Martinod, J., Guillaume, B., Regard, V., Faccenna, C., Brusset, S., 2008. Flat subduction dynamics and deformation of the South American plate: insights from analog modeling. *Tectonics* 27 (3), 1–19.
- Guo, F., Fan, W.M., Wang, Y.J., Zhang, M., 2004. Origin of early Cretaceous calc-alkaline lamprophyres from the Sulu orogen in eastern China: implications for enrichment processes beneath continental collisional belt. *Lithos* 78 (3), 291–305.
- Hacker, B.R., Ratschbacher, L., Webb, L., Ireland, T., Walker, D., Shuwen, D., 1998. U/Pb zircon ages constrain the architecture of the ultrahigh-pressure Qinling-Dabie Orogen, China. *Earth Planet. Sci. Lett.* 161, 215–230.
- He, Y.S., Li, S.G., Hoefs, J., Huang, F., Liu, S.A., Hou, Z.H., 2011. Post-collisional granitoids from the Dabie orogen: new evidence for partial melting of a thickened continental crust. *Geochim. Cosmochim. Acta* 75, 3815–3838.
- Huang, F., Li, S., Dong, F., He, Y., Chen, F., 2008. High-Mg adakitic rocks in the Dabie orogen, central China: Implications for fountaining mechanism of lower continental crust. *Chem. Geol.* 255, 1–13.
- Lee, J.K.W., Williams, I.S., Ellis, D.J., 1997. Pb, U and Th diffusion in natural zircon. *Nature* 390, 159–162.
- Li, S.G., Xiao, Y.L., Liou, D.L., Chen, Y.Z., Ge, N.J., Zhang, Z.Q., Sun, S.S., Cong, B.L., Zhang, R.Y., Stanley, R.H., Wang, S.S., 1993. Collision of the North China and Yangtze blocks and formation of coesite-bearing eclogites: timing and processes. *Chem. Geol.* 109, 89–111.
- Li, S.G., Huang, F., Nie, Y.H., Han, W.L., Long, G., Li, H.M., Zhang, Z.H., 2001. Geochemical and geochronological constraints on the suture location between the North and South China blocks in the Dabie Orogen, Central China. *Phys. Chem. Earth Part A* 26 (9), 655–672.
- Li, Y.F., Mao, J.W., Bai, F.J., Li, J.P., He, Z.J., 2003. Re-Os isotopic dating of molybdenites in Nannihu molybdenum (Tungsten) orefield in the Eastern Qinling and its geological significance. *Geol. Rev.* 49, 652–659 (in Chinese with English abstract).
- Li, Y.F., Mao, J.W., Guo, B.J., Shao, Y.J., Fei, H.C., Hu, H.B., 2004. Re-Os dating of molybdenite from the Nannihu Mo (-W) orefield in the East Qinling and its geodynamic significance. *Acta Geol. Sin.* 78, 463–470. English Edition.
- Li, X.H., Qi, C., Liu, Y., Liang, X., Tu, X.L., Xie, L., Yang, Y., 2005. Petrogenesis of the Neoproterozoic bimodal volcanic rocks along the western margin of the Yangtze Block: new constraints from Hf isotopes and Fe/Mn ratios. *Chin. Sci. Bull.* 50, 2481–2486.
- Li, Y.F., Mao, J.W., Liu, D.Y., Wang, Y.B., Wang, Z.L., Wang, Y.T., Li, X.F., Zhang, Z.H., Guo, B.J., 2006. SHRIMP zircon U-Pb and molybdenite Re-Os datings for the Leimengou porphyry molybdenum deposit, Western Henan and its geological implication. *Geol. Rev.* 52, 122–131 (in Chinese with English abstract).
- Li, X.H., Liu, Y., Li, Q.L., Guo, C.H., Chamberlain, K.R., 2009. Precise determination of Phanerozoic zircon Pb/Pb age by multicollector SIMS without external standardization. *Geochim. Geophys. Geosyst.* 10 (4), 1–21.
- Li, X.H., Long, W.G., Li, Q.L., Liu, Y., Zheng, Y.F., Yang, Y.H., Chamberlain, Kevin R., Wan, D.F., Guo, C.H., Wang, X.C., Tao, H., 2010. Penglai zircon megacrysts: a potential new working reference material for microbeam determination of Hf-O isotopes and U-Pb age. *Geostand. Geoanal. Res.* 34 (2), 117–134.
- Li, C.Y., Zhang, H., Wang, F.Y., Liu, J.Q., Sun, Y.L., Hao, X.L., Li, Y.L., Sun, W., 2012a. The formation of the Dabaoshan porphyry molybdenum deposit induced by slab rollback. *Lithos* 150, 101–110.
- Li, N., Ulrich, T., Chen, Y.J., Thomsen, T.B., Pease, V., Pirajno, F., 2012b. Fluid evolution of the Yuchiling porphyry Mo deposit, East Qinling, China. *Ore Geol. Rev.* 48, 442–459.
- Li, N., Chen, Y.J., Pirajno, F., Ni, Z.Y., 2013. Timing of the Yuchiling giant porphyry Mo system, and implications for ore genesis. *Miner. Deposita* 48, 505–524.
- Li, J., Jiang, X.Y., Xu, J.F., Zhong, L.F., Wang, X.C., Wang, G.Q., Zhao, P.P., 2014. Determination of platinum-group elements and Re-Os isotopes using ID-ICP-MS and N-TIMS from a single digestion after two-stage column separation. *Geostand. Geoanal. Res.* 38, 37–50.
- Liang, H.Y., Campbell, I.H., Allen, C., Sun, W.D., Liu, C.Q., Yu, H.X., Xie, Y.W., Zhang, Y.Q., 2006. Zircon Ce⁴⁺/Ce³⁺ ratios and ages for Yulong ore-bearing porphyries in eastern Tibet. *Miner. Deposita* 41, 152–159.
- Liang, J.L., Ding, X., Sun, X.M., Zhang, Z.M., Zhang, H., Sun, W.D., 2009. Nb/Ta fractionation observed in eclogites from the Chinese Continental Scientific Drilling Project. *Chem. Geol.* 268, 27–40.
- Lin, J., Liu, Y.S., Yang, Y.H., Hu, Z.C., 2016. Calibration and correction of LA-ICP-MS and LA-MC-ICP-MS analyses for element contents and isotopic ratios. *Solid Earth Sci.* 1 (1), 5–27.
- Ling, M.X., Wang, F.Y., Ding, X., Hu, Y.H., Zhou, J.B., Zartman, R.E., Yang, X.Y., Sun, W.D., 2009. Cretaceous ridge subduction along the lower Yangtze river belt, Eastern China. *Econ. Geol.* 104 (2), 303–321.
- Ling, M.X., Wang, F.Y., Ding, X., Zhou, J.B., Sun, W.D., 2011. Different origins of adakites from the Dabie mountains and the lower Yangtze river belt, eastern China: geochemical constraints. *Int. Geol. Rev.* 53, 727–740.
- Liu, Y., Hu, Z., Gao, S., Günther, D., Xu, J., Gao, C., Chen, H., 2008. In situ analysis of major and trace elements of anhydrous minerals by LA-ICP-MS without applying an internal standard. *Chem. Geol.* 257, 34–43.

- Liu, J., Saito, Y., Kong, X.H., Wang, H., Xiang, L.H., Wen, C., Nakashima, R., 2010. Sedimentary record of environmental evolution off the Yangtze River estuary, East China Sea, during the last~ 13,000 years, with special reference to the influence of the Yellow River on the Yangtze River delta during the last 600 years. *Quat. Sci. Rev.* 29 (17), 2424–2438.
- Lu, X.X., Yu, Z.P., Feng, Y.L., Wang, Y.T., Ma, W.F., Cui, H.F., 2002. Mineralization and tectonic setting of deep-hypabyssal granites in East Qinling molybdenum mountain. *Miner. Deposit* 21, 168–178 (in Chinese with English abstract).
- Ludington, B.S., Plumlee, G.S., Survey, U.S.G., 2009a. Climax-type porphyry molybdenum deposits. *U.S. Geol. Surv.* 1215, 1–16.
- Ludington, S., Hammarstrom, J., Piatak, N., 2009b. Low (fluorine stockwork molybdenite deposits. United States Geological Survey Open-File Rep. 1211.
- Ludwig, K.R., 2003. User's manual for Isoplot 3.00: a geochronological toolkit for Microsoft Excel. Berkeley Geochronology Centre Special Publication, California.
- Mao, J.W., Xie, G.Q., Zhang, Z.H., Li, X.F., Wang, Y.T., Zhang, C.Q., Li, Y.F., 2005. Mesozoic large-scale metallogenic pulses in North China and corresponding geodynamic setting. *Acta Petrol. Sin.* 21, 169–188 (in Chinese with English abstract).
- Mao, J.W., Xie, G.Q., Bierlein, F., Qu, W.J., Du, A.D., Ye, H.S., Pirajno, F., Li, H.M., Guo, B.J., Li, Y.F., Yang, Z.Q., 2008. Tectonic implications from Re-Os dating of Mesozoic molybdenum deposits in the East Qinling-Dabie orogenic belt. *Geochim. Cosmochim. Acta* 72, 4607–4626.
- Mao, J.W., Xie, G.Q., Pirajno, F., Ye, H.S., Wang, Y.B., Li, Y.F., Xiang, J.F., Zhao, H.J., 2010. Late jurassic-early cretaceous granitoid magmatism in Eastern Qinling, central-eastern China: SHRIMP zircon U-Pb ages and tectonic implications. *Aust. J. Earth Sci.* 57, 51–78.
- Meng, Q.R., Zhang, G.W., 1999. Timing of collision of the North and South China blocks: controversy and reconciliation. *Geology* 27 (2), 123–126.
- Meng, Q.R., Zhang, G.W., 2000. Geologic framework and tectonic evolution of the Qinling orogen, central China. *Tectonophysics* 323 (3), 183–196.
- Mi, M., Chen, Y.J., Yang, Y.F., Wang, P., Li, F.L., Wan, S.Q., Xu, Y.L., 2015a. Geochronology and geochemistry of the giant Qian'echong Mo deposit, Dabie Shan, eastern China: implications for ore genesis and tectonic setting. *Gondwana Res.* 27 (3), 1217–1235.
- Mi, M., Li, C.Y., Sun, W.D., 2015b. Qian'echong low-F porphyry Mo deposits in the Dabie Mountains, central China. *Lithos* 239, 157–169.
- Pearce, J.A., Harris, N.B.W., Tindle, A.G., 1984. Trace element discrimination diagrams for the tectonic interpretation of granitic rocks. *J. Petrol.* 25, 956–983.
- Qin, J.F., Lai, S.C., Wang, J., Li, Y.F., 2007. High-Mg# Adakitic Tonalite from the Xichahe Area, South Qinling orogenic belt (Central China): petrogenesis and geological implications. *Int. Geol. Rev.* 49 (12), 1145–1158.
- Qin, J.F., Lai, S., Li, Y., 2008. Slab breakoff model for the Triassic post-collisional adakitic granitoids in the Qinling Orogen, Central China: Zircon U-Pb ages, geochemistry, and Sr-Nd-Pb isotopic constraints. *Int. Geol. Rev.* 50 (12), 1080–1104.
- Qin, J.F., Lai, S.C., Grapes, R., Diwu, C.R., Ju, Y.J., Li, Y.F., 2009. Geochemical evidence for origin of magma mixing for the Triassic monzonitic granite and its enclaves at Mishuling in the Qinling orogen (central China). *Lithos* 112 (3), 259–276.
- Qin, J.F., Lai, S.C., Grapes, R., Diwu, C.R., Ju, Y.J., Li, Y.F., 2010. Origin of LateTriassic high-Mg adakitic granitoid rocks from the Dongjiangkou area, Qinling orogen, central China: implications for subduction of continental crust. *Lithos* 120 (3), 347–367.
- Sillitoe, R.H., 1980. Types of porphyry molybdenum deposits. *Min. Mag.* 142 (6), 550–553.
- Sláma, J., Košler, J., Condon, D.J., Crowley, J.L., Gerdes, A., Hanchar, J.M., Horstwood, M.S.A., Morris, G.A., Nasdala, L., Norberg, N., Schaltegger, U., Schoene, B., Tubrett, M.N., Whitehouse, M.J., 2008. Plešovice zircon—a new natural reference material for U-Pb and Hf isotopic microanalysis. *Chem. Geol.* 249, 1–35.
- Sobolev, Stephan V., Yu Babeyko, A., 2005. What drives orogeny in the Andes? *Geology* 33 (8), 617–620.
- Stacey, J.S., Kramers, J.D., 1975. Approximation of terrestrial lead isotope evolution by a two-stage model. *Earth Planet. Sci. Lett.* 26, 207–221.
- Stein, H.J., Markey, R.J., Morgan, J.W., Du, A., Sun, Y., 1997. Highly precise and accurate Re-Os ages for molybdenite from the east qinling molybdenum belt, Shaanxi Province, China. *Econ. Geol.* 92, 827–835.
- Sun, W., Li, S., Chen, Y., Li, Y., 2002a. Timing of synorogenic granitoids in the South Qinling, Central China: constraints on the evolution of the Qinling-Dabie Orogenic Belt. *J. Geol.* 110 (4), 457–468.
- Sun, W., Williams, I.S., Li, S., 2002b. Carboniferous and Triassic eclogites in the western Dabie Mountains, east-central China: evidence for protracted convergence of the North and South China Blocks. *J. Metamorph. Geol.* 20, 873–886.
- Sun, W., Ding, X., Hu, Y.H., Li, X.H., 2007. The golden transformation of the cretaceous plate subduction in the west pacific. *Earth Planet. Sci. Lett.* 262 (3), 533–542.
- Sun, W., Ling, M., Yang, X., Fan, W., Ding, X., Liang, H., 2010. Ridge subduction and porphyry copper-gold mineralization: an overview. *Sci. China Earth Sci.* 53 (4), 475–484.
- Sun, W.D., Li, C.Y., Hao, X.L., Ling, M.X., Ireland, T., Ding, X., Fan, W.M., 2016. Oceanic anoxic events, subduction style and molybdenum mineralization. *Solid Earth Sci.* 1 (2), 64–73.
- Tu, X.L., Zhang, H., Deng, W.F., Ling, M.X., Liang, H.Y., Liu, Y., Sun, W.D., 2011. Application of RESolution in-situ laser ablation ICP-MS in trace element analyses. *Geochimica* 40, 83–98.
- Wang, Q., Wyman, D.A., Xu, J.F., Jian, P., Zhao, Z.H., Li, C.F., Xu, W., Ma, J.L., He, B., 2007. Early Cretaceous adakitic granites in the Northern Dabie Complex, central China: implications for partial melting and delamination of thickened lower crust. *Geochim. Cosmochim. Acta* 71 (10), 2609–2636.
- Wang, P., Yang, Y.F., Mei, M., Li, Z.L., Wang, L.J., 2013. Fluid evolution of the Yaochong porphyry Mo deposit, Xinxiang County, Henan Province. *China Acta Petrol. Sin.* 29 (1), 107–120.
- Wang, P., Chen, Y.J., Fu, B., Yang, Y.F., Mi, M., Li, Z.L., 2014. Fluid inclusion and H-O-C isotope geochemistry of the Yaochong porphyry Mo deposit in Dabie Shan, China: a case study of porphyry systems in continental collision orogens. *Int. J. Earth Sci.* 103, 777–797.
- Wang, P., Wang, Y., Yang, Y.F., 2017. Zircon U-Pb geochronology and isotopic geochemistry of the Tangjiaping Mo deposit, Dabie Shan, eastern China: implications for ore genesis and tectonic setting. *Ore Geol. Rev.* 81 (2), 466–483.
- Wiedenbeck, M., Alle, P., Corfu, F., Griffin, W.L., Meier, M., Oberli, F., von Quadt, A., Roddick, J.C., Spiegel, W., 1995. Three natural zircon standards for U-Th-Pb, Lu-Hf, trace element and REE analyses. *Geostandards Newslett.* 19, 1–23.
- Yang, Y.F., Li, N., Chen, Y.J., 2012. Fluid inclusion study of the Nannihu giant porphyry Mo-W deposit, Henan Province, China: implications for the nature of porphyry ore-fluid systems formed in a continental collision setting. *Ore Geol. Rev.* 46, 83–94.
- Zhang, R.Y., Liou, J.G., Ernst, W.G., 2009. The Dabie-Sulu continental collision zone: a comprehensive review. *Gondwana Res.* 16, 1–26.
- Zhang, H., Li, C., Yang, X., Sun, Y., Deng, J., Wang, R., Wang, B., Wang, Y., Sun, W., 2013. Shapinggou : the largest Climax-type porphyry Mo deposit in China. *Int. Geol. Rev.*, 1–19
- Zhang, H., Li, C., Yang, X., Sun, Y., Deng, J., Wang, R., Wang, B., Wang, Y., Sun, W., 2014. Shapinggou : the largest Climax-type porphyry Mo deposit in China. *Int. Geol. Rev.*, 37–41
- Zhao, Z.F., Zheng, Y.F., Wei, C.S., Wu, F.Y., 2011. Origin of postcollisional magmatic rocks in the Dabie orogen: implications for crust-mantle interaction and crustal architecture. *Lithos* 126, 99–114.
- Zheng, Y., 2008. A perspective view on ultrahigh-pressure metamorphism and continental collision in the Dabie-Sulu orogenic belt. *Chin. Sci. Bull.* 53, 3081–3104.
- Zheng, Y.F., Fu, B., Gong, B., Li, L., 2003. Stable isotope geochemistry of ultrahigh pressure metamorphic rocks from the Dabie – Sulu orogen in China: implications for geodynamics and fluid regime. *Earth Sci. Rev.* 62, 105–161.
- Zhou, J.B., Wilde, S.A., Zhao, G.C., Zheng, C.Q., Jin, W., Zhang, X.Z., Cheng, H., 2008. Detrital zircon U-Pb dating of low-grade metamorphic rocks in the Sulu UHP belt: evidence for overthrusting of the North China Craton onto the South China Craton during continental subduction. *J. Geol. Soc.* 165 (1), 423–433.